Observations of grain-size sensitive power-law creep of olivine aggregates over a large range of lattice-preferred orientation strength

Jacob A. Tielke,[1] Lars N. Hansen,[2] Miki Tasaka,[1] Cameron Meyers,[1] Mark E. Zimmerman,[1] and David L. Kohlstedt[1]

Corresponding author: J. A. Tielke, Department of Earth Sciences, University of Minnesota, 310 Pillsbury Drive SE, Minneapolis, MN 55455, USA. (tielk003@umn.edu)

[1]Department of Earth Sciences,
University of Minnesota, Minneapolis,
Minnesota, USA.

[2]Department of Earth Sciences,
University of Oxford, Oxford, England, UK.

This article has been accepted for publication and undergone full peer review but has not been through the copyediting, typesetting, pagination and proofreading process, which may lead to differences between this version and the Version of Record. Please cite this article as doi: 10.1002/2015JB012302

Abstract. Grain-size sensitive (GSS) power-law creep of San Carlos olivine aggregates was investigated by comparing strain rates measured in laboratory deformation experiments to strain rates determined from a micromechanical model of intragranular dislocation processes. The plastic flow behavior of olivine aggregates due solely to intragranular slip was determined using flow laws for olivine single crystals in combination with grain orientations measured by electron-backscatter diffraction. Measured strain rates were compared to results from the micromechanical model for samples deformed in compression to an axial strain of <0.2 and in torsion to a shear strain of up to 7.4. Olivine aggregates deform up to a factor of 4.6 times faster than the maximum possible rates determined from the micromechanical model of intragranular slip. Comparison of our data to published flow laws indicates that diffusion creep cannot account for this difference. The ratio of experimentally determined strain rates to those from the micromechanical model is strongly dependent upon grain size, but is independent of stress and strength of lattice-preferred orientation. These observations indicate that GSS power-law creep, consistent with dislocation-accommodated grain-boundary sliding, occurs in both weakly and strongly textured olivine aggregates at the studied conditions.

1. Introduction

Geodynamic simulations of solid-state flow in the upper mantle require flow laws derived from experimental deformation of olivine-rich rocks. These flow laws define rheological regimes, which describe conditions at which the mechanical behavior of materials behave in a defined manner. An important aspect of experimental deformation is relating flow laws to deformation mechanisms that describe the atomistic process that give rise to flow [*Frost and Ashby*, 1982]. Multiple deformation mechanisms may operate simultaneously during high-temperature deformation. The relative influence of each mechanism depends upon state variables including grain size, stress, and strength of lattice-preferred orientation (LPO) [*Evans*, 2005], each of which may vary significantly between laboratory and upper-mantle conditions. It is therefore possible that the dominant deformation mechanism at laboratory conditions is not the dominant mechanism under mantle conditions, a situation that would result in significant error in geodynamic simulations. To evaluate the contributions of different deformation mechanisms operating during polycrystalline deformation, we compared strain rates measured in deformation experiments on olivine aggregates to strain rates determined from a micromechanical model.

The micromechanical model used in this paper allows for isolation of the contribution of the motion of lattice dislocations, a grain size insensitive (GSI) process, to the total strain rate of an aggregate. This step is carried out by combining crystallographic orientation data from deformation experiments on olivine aggregates with flow laws for individual slip systems obtained from high-temperature creep experiments on olivine single crystals. We compare strain rates determined from the micromechanical model to strain rates

measured from experimentally deformed samples to quantify the influence of grain-size sensitive (GSS) processes. These data are then used to identify the dominant deformation mechanism that is operating at different conditions of grain size, stress, and strength of LPO.

Multiple rheological regimes have been identified during high-temperature steady-state deformation of olivine aggregates. These regimes include GSS linear creep, GSS power-law creep, and GSI power-law creep. The steady-state rheological behavior of olivine aggregates under high-temperature conditions is well described by flow laws of the form

$$\dot{\varepsilon} = A\frac{\sigma^n}{d^p} f_{\mathrm{O}_2}^{\ m} f_{\mathrm{H_2O}}^{r} \exp\left(\frac{-Q}{\mathrm{R}T}\right), \tag{1}$$

where $\dot{\varepsilon}$ is strain rate, A is a material specific parameter, σ is differential stress, n is the stress exponent, d is grain size, p is the grain size exponent, f_{O_2} is oxygen fugacity, m is the oxygen fugacity exponent, $f_{\mathrm{H_2O}}$ is water fugacity, r is the water fugacity exponent, Q is activation enthalpy, R is the gas constant, and T is temperature. If the rheological regimes represent deformation mechanisms that operate independently of one another, the total strain rate for a viscously deforming aggregate, $\dot{\varepsilon}_{\mathrm{total}}$, can be expressed as a constitutive equation of the form

$$\dot{\varepsilon}_{\mathrm{total}} = \dot{\varepsilon}_{\mathrm{GSS\text{-}linear}} + \dot{\varepsilon}_{\mathrm{GSS\text{-}power}} + \dot{\varepsilon}_{\mathrm{GSI\text{-}power}}, \tag{2}$$

where the subscripts GSS-linear, GSS-power, and GSI-power refer to the strain rates from GSS linear creep, GSS power-law creep, and GSI power-law regimes, respectively.

The flow law parameters that define individual rheological regimes of a plastically deforming olivine aggregate may be used to infer the dominant, or rate-controlling, defor-

mation mechanism operating in each regime. During GSS linear creep, n equals 1 and p equals 2 or 3, and deformation occurs by a diffusion mechanism [*Nabarro*, 1948; *Herring*, 1950; *Coble*, 1963]. GSS power-law creep occurs when n is greater than 1 and p is greater than 0, and indicates deformation occurs by a mechanism that involves the motion of lattice dislocations aided by deformation associated with the migration of and displacement along grain boundaries [*Langdon*, 1994]. GSI power-law creep occurs when values of n are 3 to 4 and values of p are 0 and indicates that dislocation creep is dominant [*Poirier*, 1985, p. 103-109]. The dominant deformation mechanisms operating during GSS linear creep and GSI power-law creep are well agreed upon. However, the deformation mechanism operating during the GSS power-law regime of olivine aggregates has been attributed to dislocation-accommodated grain boundary sliding (disGBS) [*Hirth and Kohlstedt*, 2003; *Drury*, 2005; *Hansen et al.*, 2011, 2012] or dynamic recrystallization-controlled (DRX) dislocation creep [*Platt and Behr*, 2011; *Johanesen and Platt*, 2015].

The dominant deformation mechanism may also be inferred from microstructural observations of deformed rocks. Typically, a strong LPO is interpreted as evidence of dislocation creep, while a weak LPO or nearly random orientation distribution is interpreted as evidence of diffusion creep [e.g., *Warren and Hirth*, 2006; *Mehl and Hirth*, 2008; *Toy et al.*, 2010]. However, determination of the dominant deformation mechanism based on microstructural observations is not always straightforward. In olivine aggregates that were experimentally deformed in GSS linear and GSS power law regimes, LPOs of various strength have been observed. For example, a LPO has been observed in very fine-grained olivine aggregates deformed at low differential stress with n close to 1, suggesting fabric development may occur when diffusion creep is the dominant deformation mechanism

[*Miyazaki et al.*, 2013; *Sundberg and Cooper*, 2008]. Similarly, a LPO has been observed in olivine aggregates in which n is approximately 3 and p equals 0.7 [*Hansen et al.*, 2011], indicating that a LPO develops during GSS power-law creep.

In naturally deformed mantle rocks interpreted to have deformed by both GSS linear and GSS power-law creep, a LPO has also been observed. Lherzolite deformed at lithospheric mantle conditions displays a weak olivine LPO at conditions of stress and grain size near the transition from GSS linear to GSS power-law creep [*Drury et al.*, 2011]. Peridotite deformed at conditions consistent with GSS power-law creep develops an LPO whose strength and orientation correlates with grain size [*Précigout and Hirth*, 2014]. Numerical simulations indicate that mantle materials retain a preexisting LPO after deformation via GSS linear creep [*Wheeler*, 2009], further complicating the interpretation of observations of LPO in the field.

These observations highlight the need for a method, in addition to experimentally determined flow law parameters and observation of microstructure, to infer the activity of individual deformation mechanisms in deformed rocks. In this paper, results from a micromechanical model are compared to measurements of strain rate from experimentally deformed olivine aggregates to investigate the operation of GSS power-law creep as a function of grain size, stress, and LPO strength. This process provides an additional tool to investigate the nature of the deformation mechanism that operates during GSS power-law creep of olivine aggregates.

2. Methods

Mechanical and crystallographic orientation data from experiments on olivine aggregates deformed in triaxial compression, general shear (samples sheared between pistons

cut at 45° to the compression direction), or torsion were utilized for the micromechanical model. The starting material for all experiments consisted of dried powders of San Carlos olivine that were uniaxially cold pressed at 100 MPa pressure and room temperature and then isostatically hot pressed at 300 MPa and 1200 or 1250°C. During the hot press and deformation portion of the experiments, the samples were surrounded by a nickel sleeve to control oxygen fugacity at the Ni/NiO buffer.

Values of grain size were determined from EBSD analyses of deformed samples using the MTEX toolbox for MATLAB® [*Bachmann et al.*, 2010]. Examples of typical EBSD maps used to quantify grain size and LPO are presented in Figure 1. Step sizes used for EBSD mapping were between 0.25 and 1.0 μm and a critical misorientation angle of 10° was used to separate grains. Clusters of less than 5 pixels were omitted from calculations of grain size values for each sample. The mean grain size for each sample was determined by taking the arithmetic mean of the equivalent diameter of the grains calculated from the area. Values of grain size for each sample are well fit by a log-normal distribution. The mean value was then multiplied by a factor of 1.5 to correct for artifacts introduced by the non-spherical nature of olivine grains as described by *Underwood* [1970, p. 80-93].

The steady-state values of stress and strain rate at the last segment of deformation of each experiment were used in the micromechanical model. Therefore, measurements of crystallographic fabric and grain size directly correspond with the mechanical data. A uniform stress condition is assumed such that the strain rate of each grain is calculated from the orientation of the dislocation slip systems with respect to the applied stress. This simplifying assumption yields the fastest possible estimates of strain rate from the motion of dislocations and, therefore, the smallest possible estimates of the contribution of GSS

deformation mechanisms to the total strain rate of an aggregate. The strain rate from dislocation creep for each grain in a deformed aggregate is estimated using published single crystal flow laws combined with the crystallographic orientation of the grain determined from EBSD.

The stress tensor in the sample reference frame for triaxial compression, $\boldsymbol{\sigma}_{\mathrm{t}}$, is

$$\boldsymbol{\sigma}_{\mathrm{t}} = \begin{bmatrix} \sigma_{\mathrm{A}} + P_c & 0 & 0 \\ 0 & P_c & 0 \\ 0 & 0 & P_c \end{bmatrix} \tag{3}$$

and the stress tensor in the sample reference frame for torsion or general shear experiments, $\boldsymbol{\sigma}_{\mathrm{s}}$, is

$$\boldsymbol{\sigma}_{\mathrm{s}} = \begin{bmatrix} P_c & \sigma_{\mathrm{A}} & 0 \\ \sigma_{\mathrm{A}} & P_c & 0 \\ 0 & 0 & P_c \end{bmatrix}, \tag{4}$$

where σ_A is the applied stress and P_c is the confining pressure. Either stress tensor can then be rotated into the crystallographic reference frame, as indicated by the prime symbol, by $\boldsymbol{\sigma}' = \boldsymbol{R}^{\mathrm{T}}\, \boldsymbol{\sigma}\, \boldsymbol{R}$, where $\boldsymbol{R}$ is the rotation matrix defining the orientation of the crystal reference frame relative to the sample reference frame.

The symmetric glide tensor, $\boldsymbol{\mu}^{\alpha}$, for each slip system ($\alpha$) is determined from the relation

$$\boldsymbol{\mu}^{\alpha} = \frac{1}{2}\left(b_i^{\alpha} n_j^{\alpha} + b_j^{\alpha} n_i^{\alpha}\right), \tag{5}$$

where b is the Burgers vector and n is a unit vector normal to the slip plane for each slip system [*Lebensohn and Tomé*, 1993]. The shear stress resolved onto each slip system, τ^{α}, is calculated by

$$\tau^{\alpha} = \boldsymbol{\mu}^{\alpha} : \boldsymbol{S}', \tag{6}$$

where the deviatoric stress tensor, $\boldsymbol{S}'$, is

$$\boldsymbol{S}' = \begin{bmatrix} \sigma_{11} - \sigma_{\mathrm{m}} & \sigma_{12} & \sigma_{13} \\ \sigma_{21} & \sigma_{22} - \sigma_{\mathrm{m}} & \sigma_{23} \\ \sigma_{31} & \sigma_{32} & \sigma_{33} - \sigma_{\mathrm{m}} \end{bmatrix}, \tag{7}$$

and $\sigma_{\mathrm{m}} = \frac{1}{3}\mathrm{trace}(\boldsymbol{\sigma}')$.

Once the differential stress on each slip system, $\Delta\sigma^{\alpha}$, is determined from

$$\Delta\sigma^{\alpha} = |2\tau^{\alpha}|, \tag{8}$$

the strain rate due to dislocation glide is calculated. The strain rate due to glide, $\dot{\varepsilon}_g^{\alpha}$, on each slip system is then calculated using the flow laws from Table 4 of *Bai et al.* [1991] for olivine single crystals deforming by dislocation creep, which is

$$\dot{\varepsilon}_{\mathrm{g}}^{\alpha} = \dot{\varepsilon}_{\mathrm{g}}^{\alpha}\left(\Delta\sigma^{\alpha},\, T, f_{\mathrm{O_2}}\right) \mathrm{sgn}\left(\tau^{\alpha}\right), \tag{9}$$

where $\mathrm{sgn}\left(\tau^{\alpha}\right)$ indicates the sign (positive or negative) of the value of the resolved shear stress on the given slip system. The $[110]_{\mathrm{c}}$, $[101]_{\mathrm{c}}$, and $[011]_{\mathrm{c}}$ orientations were assumed to deform by operation of the (010)[100], (001)[100], and (010)[001] slip systems, respectively. To calculate the total strain rate due to glide in each grain, shear strain rates from glide, $\dot{\gamma_g^{\alpha}}$, are required:

$$\dot{\gamma_g^{\alpha}} = 2\,\dot{\varepsilon}_g^{\alpha}. \tag{10}$$

The strain rate tensor for glide in the crystallographic reference frame, $\dot{\boldsymbol{\varepsilon}}_g'$, is determined for each grain by summing the contribution from all of the slip systems:

$$\dot{\boldsymbol{\varepsilon}}'_g = \sum_{\alpha=1}^{3} \boldsymbol{\mu}^{\alpha}\dot{\gamma}_g^{\alpha}. \tag{11}$$

To calculate the strain rate of the aggregate, the strain rate tensor must be rotated back into the sample reference frame. The strain rate tensor for each grain in the sample reference frame, $\dot{\boldsymbol{\varepsilon}}_{\text{grain}}$, is

$$\dot{\boldsymbol{\varepsilon}}_{\text{grain}} = \mathrm{R}^{\mathrm{T}} \ \dot{\boldsymbol{\varepsilon}}'_g \, \mathrm{R} = \begin{bmatrix} \dot{\varepsilon}_{11} & \dot{\varepsilon}_{12} & \dot{\varepsilon}_{13} \\ \dot{\varepsilon}_{21} & \dot{\varepsilon}_{22} & \dot{\varepsilon}_{23} \\ \dot{\varepsilon}_{31} & \dot{\varepsilon}_{32} & \dot{\varepsilon}_{33} \end{bmatrix}. \tag{12}$$

Assuming a uniform stress state and ignoring strain compatibility, we estimate the fastest possible volume-averaged strain rate from intragranular deformation from

$$\dot{\boldsymbol{\varepsilon}} = \frac{\sum_{\alpha=1}^{\mathrm{N}} \dot{\boldsymbol{\varepsilon}}^{\alpha}_{\text{grain}} V^{\alpha}_{\text{grain}}}{\sum_{\alpha=1}^{\mathrm{N}} V^{\alpha}_{\text{grain}}}, \tag{13}$$

where V_{grain} is the volume of each grain. The calculated value of the equivalent strain rate due to dislocation creep using the measured crystallographic orientations from deformation experiments, $\dot{\varepsilon}_{\,\text{dis}}$, is

$$\dot{\varepsilon}_{\,\text{dis}} = \sqrt{\frac{2}{3} \, \dot{\varepsilon}_{\,ij} \, \dot{\varepsilon}_{\,ji}} \,, \tag{14}$$

which allows for comparison between experiments carried out in different deformation geometries. Values of $\dot{\varepsilon}_{\,\text{dis}}$ were calculated using both the set of grain orientations as determined from EBSD analyses, $\dot{\varepsilon}_{\,\text{calc-fabric}}$, and a set of grain orientations randomly drawn from a uniform distribution, $\dot{\varepsilon}_{\,\text{calc-uni}}$, generated from a large population of random grain orientations.

3. Results

Calculated values of equivalent strain rate for individual grains determined from Equation 12 depend upon grain orientation, as illustrated in Figure 2. The grains with the

largest values of resolved shear stress on (010)[100] ($RSS_{(010)[100]}$) have the highest values and smallest range of calculated equivalent strain rate. Grains that have the smallest values of $RSS_{(010)[100]}$ generally have lower values and a larger range of calculated equivalent strain rate.

The primary microstructural difference between samples deformed in triaxial compression to those deformed in general shear and torsional shear is the strength and geometry of the LPO as presented in Figure 3. For the case of compression, the [010] axes align preferentially with the compression axis, and the [100] and [001] axes form a girdle perpendicular to the orientation of the compression axis. For general shear and torsion experiments, the [100] axes preferentially align in the direction of shear, and the [010] and [001] axes form a girdle around the direction of shear that is associated with a maximum of [010] perpendicular to the shear plane. Values for the J-index, a measure of fabric strength [*Bunge*, 1982], range from 1.2 for compression experiments and up to 5.5 for torsion experiments.

To quantify the difference between the measured strain rate, $\dot{\varepsilon}_{\text{meas}}$, and $\dot{\varepsilon}_{\text{calc-fabric}}$, we define the strain rate enhancement factor, f, as

$$f = \frac{\dot{\varepsilon}_{\text{meas}}}{\dot{\varepsilon}_{\text{calc-fabric}}} \,. \tag{15}$$

Measured and calculated values of strain rate and associated values of f are presented in Table 1. The values of f vary as a function of grain size, but are nearly independent of stress and LPO, as illustrated in Figure 4. A least-squares fit of f as a function of grain size measured at the end of each experiment yields

$$f = 10^{1.1 \pm 0.6} d^{-1.0 \pm 0.7} \,, \tag{16}$$

where d is the grain size in 10^{-6} m.

4. Discussion

The values of f presented in Table 1 indicate that the strain rates obtained from the micromechanical model are often significantly slower than those measured experimentally over a large range of conditions of grain size, stress, and LPO strength. Calculations of aggregate plasticity can be made using end-member models (uniform stress versus uniform strain rate) to bound the most realistic scenarios [e.g., *Dawson and Wenk*, 2000]. Here we made the simplifying assumption that all grains were subject to the same stress state [*Sachs*, 1928], which ignores compatibility requirements. This end-member model describes the fastest strain rates possible with purely intragranular plasticity. Although more sophisticated grain-scale micromechanical models are available, such as those described by *Lebensohn and Tomé* [1993], we have taken the most conservative approach to characterizing the discrepancies between experiments and calculations.

A consequence of using the uniform stress bound in our calculations is that values of $f < 1$ are possible even when deformation occurs in a GSS creep regime. To approximate the lowest possible values of f that still reflect deformation in a GSS regime, the micromechanical model was applied to experiments carried out on Åheim dunite with a mean grain size of ∼900 μm [*Keefner et al.*, 2011]. The large grain size of the sample analyzed from that study results in a negligible contribution from GSS deformation at the experimental conditions and therefore yields approximate values of f for deformation occurring in the GSI regime. Calculated values of f from a coarse grained dunite (PI3-1166) are 0.5 or 0.7 using either a nearly uniform distribution of grain orientations or a small sample size of grain orientations from EBSD measurements of the deformed sample,

respectively. Therefore, the transition from GSI to GSS creep likely occurs near values of f of 0.5 to 0.7.

In light of these observations, it is clear that the experimentally measured strain rate cannot be accounted for by the activity of intragranular dislocations alone. As illustrated in Figure 4a, the ratio of the measured to calculated strain rates increases with decreasing grain size, implying that a grain-size sensitive deformation mechanism is operating. Published flow laws for olivine aggregates [*Hansen et al.*, 2011; *Hirth and Kohlstedt*, 2003] demonstrate that strain rates due to diffusion creep (a grain-size sensitive mechanism) at the conditions of these experiments account for only 0.1 to 21% of the measured strain rates; thus diffusion creep cannot be responsible for the observed discrepancies. Furthermore, values of stress exponents measured by load-stepping sequences in triaxial compression experiments and rate-stepping excursions in torsion experiments are between 2 and 4, indicating the importance of the motion of dislocations to the strain rate. The combination of high values of n and observed grain-size sensitivity indicate deformation occurred in the GSS power-law rheological regime.

One mechanism proposed to account for GSS power-law creep of quartz [*Platt and Behr*, 2011] and olivine [*Johanesen and Platt*, 2015] is dynamic recrystallization (DRX) controlled dislocation creep. In this creep regime, strain-induced grain boundary migration acts to grow grains with low dislocation densities at the expense of those with high dislocation densities. This process works to counteract strain hardening induced by dislocation-dislocation interactions within grains. *Johanesen and Platt* [2015] argue that this mechanism was operating in exhumed peridotite shear zones, largely because curved and lobate grain boundaries are taken to indicate high rates of grain-boundary migration.

Microstructural observations from laboratory experiments argue against DRX controlled creep as the primary mechanism operating during high-temperature deformation of olivine aggregates. Analyses of experimentally deformed olivine aggregates indicate that grains with the largest dislocation densities are those with the largest Schmid factor for the (010)[100] dislocation slip system in both low strain compression experiments [*Farla et al.*, 2011] and higher strain general shear experiments [*Lee et al.*, 2002]. Thus, one would expect that strain driven grain boundary migration selectively removes grains that are well orientated with respect to the externally applied stress for deformation on the (010)[100] dislocation slip system. If DRX controlled creep were the dominant mechanism operating during deformation, migration of grain boundaries would create an aggregate with either a random LPO or a LPO with a maximum of [001] parallel to the shear direction. We therefore conclude that although DRX creep may be important during low-temperature deformation, observations of the LPOs that develop during anhydrous deformation of olivine aggregates argue against its importance at high-temperature conditions.

Dislocation-accommodated GBS (disGBS) has been identified as an important deformation mechanism in olivine aggregates based on experiments performed in the GSS power-law rheological regime [*Hirth and Kohlstedt*, 1995, 2003; *Wang et al.*, 2010; *Hansen et al.*, 2011]. Similar behavior has been documented in other geological materials including calcite [*Schmid et al.*, 1977; *Walker et al.*, 1990] and ice [*Goldsby and Kohlstedt*, 2001]. The results of these studies are in good agreement with theoretical models of grain-boundary sliding accommodated by the motion of intragranular dislocations as described by *Langdon* [1994].

In contrast to the incompatibility of DRX controlled creep with observed LPOs, disGBS is compatible with the nature and strength of the LPO observed in samples deformed in laboratory experiments. During disGBS, displacements along grain boundaries are coupled with the motion of lattice dislocations in adjacent grains [*Hirth and Kohlstedt*, 2003]. This coupling results in a significant contribution of intracrystalline dislocation processes to the strain rate of a deforming aggregate and therefore to the rotation and preferred alignment of individual grains. Observations of LPO development during GSS power-law creep [e.g., *Hansen et al.*, 2012, 2014] are consistent with this process. The similarities between observations of LPO in olivine aggregates deformed during GSS power-law creep and those predicted from models of GSI power-law creep [e.g., *Tommasi et al.*, 2000; *Kaminski and Ribe*, 2001; *Castelnau et al.*, 2009] are consistent with significant operation of intracrystalline dislocation processes during disGBS.

Laboratory-derived flow laws for GSS power-law creep have values of n between those for diffusion creep and dislocation creep. This observation suggests that GSS power-law creep may be due to simultaneous operation of diffusion and dislocation creep. However, the results presented in Figure 4 indicate the observed GSS power-law regime is attributed to the operation of one deformation mechanism. If the rheological behavior attributed to disGBS were actually only the result of simultaneous operation of diffusion creep and dislocation creep, then one would expect the LPOs observed at high-strain conditions in Figure 3, which promote an increase in the resolved shear stress acting upon the weakest dislocation slip system, to promote dislocation creep over diffusion creep. In this scenario, increasing the strength of the crystallographic fabric would result in a significant decrease of the contribution of grain-size sensitive deformation to the total strain rate, a situation

that would result in a strong decrease in f with increasing LPO strength. In contrast, the results presented in Figure 4b indicate that values of f, which describe the contribution of grain size sensitive deformation, remain essentially constant with increasing LPO strength.

The results presented in Figure 4c indicate that f is not dependent on stress for the studied experimental conditions. This result is also consistent with the operation of all of the experiments in one rheological regime. If the observed GSS mechanism were the result of a combination of two processes, the values of f would decrease with increasing stress, which is not observed. Therefore, disGBS must be a separate deformation mechanism rather than a transition between diffusion creep and dislocation creep. This conclusion is supported by the experimentally derived flow laws for olivine aggregates presented in Figure 5, where it is apparent that the strain rate from the disGBS flow law cannot be explained by a combination of the diffusion and dislocation creep flow laws. If the strain rate from disGBS were actually due to a combination of diffusion and dislocation creep, the dashed line, which represents a combination of diffusion creep and dislocation creep in Figure 5, would correspond with the solid line representing disGBS. However, the dashed line is a factor of 6 lower in strain rate than the disGBS flow law for the stress at which the diffusion and dislocation creep flow laws intersect.

Goldsby and Kohlstedt [2001], based on experiments on ice, and *Hirth and Kohlstedt* [2003], based on experiments on olivine, suggested that the strain rate of the disGBS mechanism is limited by either the strain rate from displacement along grain boundaries ($\dot{\varepsilon}_{\mathrm{GBS}}$) or the strain rate from the weakest dislocation slip system ($\dot{\varepsilon}_{\mathrm{easy}}$). Comparison of values of $\dot{\varepsilon}_{\mathrm{easy}}$ determined from the flow laws of *Bai et al.* [1991] and $\dot{\varepsilon}_{\mathrm{GBS}}$ estimated from the analyses of *Jackson et al.* [2014] indicates that $\dot{\varepsilon}_{\mathrm{easy}} \approx 10^{-6}\,\dot{\varepsilon}_{\mathrm{GBS}}$ for the experimental

conditions used in this study. Therefore, $\dot{\varepsilon}_{\text{disGBS}}$ would be expected not to surpass $\dot{\varepsilon}_{\text{easy}}$. This relationship is consistent with the observations presented in Figure 6. As the value of the J-index increases, $\dot{\varepsilon}_{meas}$ / $\dot{\varepsilon}_{easy}$ increases rapidly. However, for a value of J-index greater than ∼2, $\dot{\varepsilon}_{meas}$ / $\dot{\varepsilon}_{easy}$ remains relatively constant at approximately unity. This observation is consistent with deformation that is rate limited by the strength of the weakest dislocation slip system. The implication of these observations is that the strain rate of olivine aggregates deforming by the disGBS mechanism will approach the strain rate of the weakest slip systems once an LPO has developed. However, if deformation is indeed limited by $\dot{\varepsilon}_{\text{easy}}$, it remains to be demonstrated that strain rate is independent of grain size and exhibits the same activation energy as observed for olivine single crystals oriented for easy slip.

5. Conclusions

Our analysis demonstrates that the observed strain rate in deformation experiments of olivine aggregates cannot be explained by the operation of intragranular dislocation or diffusion mechanisms alone. A deformation mechanism that is both grain-size sensitive and has a power-law dependence of strain rate upon stress must operate. The independence of values of f on stress and fabric strength indicates a simple combination of diffusion creep and dislocation creep cannot account for the observed strain rate. Therefore, disGBS operates in olivine aggregates over a large range of conditions of stress and crystallographic fabric strength.

Acknowledgments. This work benefited greatly from conversations with Amanda Dillman. The manuscript was much improved by thoughtful reviews by Greg Hirth and

an anonymous reviewer. This research was supported by NASA Solar Systems Workings grant NNX15AL53G and NSF EAR grant 1214876. Parts of this work were carried out in the Characterization Facility, University of Minnesota, which receives partial support from NSF through the MRSEC program. Data used in these analyses can be obtained by emailing the corresponding author.

References

Bachmann, F., R. Hielscher, and H. Schaeben (2010), Texture analysis with mtex–free and open source software toolbox, *Sol. St. Phen.*, *160*, 63–68.

Bai, Q., S. Mackwell, and D. Kohlstedt (1991), High-temperature creep of olivine single crystals 1. Mechanical results for buffered samples, *J. Geophys. Res.*, *96*, 2441–2463.

Bunge, H. (1982), *Texture analysis in materials science*, Butterworths, Boston.

Castelnau, O., D. K. Blackman, and T. W. Becker (2009), Numerical simulations of texture development and associated rheological anisotropy in regions of complex mantle flow, *Geophys. Res. Lett.*, *36*, L12304.

Coble, R. (1963), A model for boundary diffusion controlled creep in ceramic materials, *J. App. Phys.*, *34*(6), 1679–1682.

Dawson, P. R., and H.-R. Wenk (2000), Texturing of the upper mantle during convection, *Philos. Mag. A*, *80*(3), 573–598.

Drury, M. (2005), Dynamic recrystallization and strain softening of olivine aggregates in the laboratory and the lithosphere, *Geo. Soc. Lond. Spec. Publ.*, *243*(1), 143.

Drury, M., H. A. Lallemant, G. Pennock, and L. Palasse (2011), Crystal preferred orientation in peridotite ultramylonites deformed by grain size sensitive creep, étang de lers,

pyrenees, france, *J. Struct. Geol.*, *33*(12), 1776–1789.

Evans, B. (2005), Creep constitutive laws for rocks with evolving structure, *Geological Society, London, Special Publications*, *245*(1), 329–346.

Farla, R., J. F. Gerald, H. Kokkonen, A. Halfpenny, U. Faul, and I. Jackson (2011), Slip-system and ebsd analysis on compressively deformed fine-grained polycrystalline olivine, *Geological Society, London, Special Publications*, *360*(1), 225–235.

Frost, H., and M. Ashby (1982), *Deformation Mechanism Maps*, Pergamon Press, New York.

Goldsby, D., and D. Kohlstedt (2001), Superplastic deformation of ice: Experimental observations, *J. Geophys. Res.*, *106*, 11017–11030.

Hansen, L., M. Zimmerman, and D. Kohlstedt (2012), The influence of microstructure on deformation of olivine in the grain-boundary sliding regime, *J. Geophys. Res.*, *117*, B09201.

Hansen, L. N., M. E. Zimmerman, and D. L. Kohlstedt (2011), Grain-boundary sliding in San Carlos olivine: Flow-law parameters and crystallographic-preferred orientation, *J. Geophys. Res.*, *116*, B08201.

Hansen, L. N., Y.-H. Zhao, M. E. Zimmerman, and D. L. Kohlstedt (2014), Protracted fabric evolution in olivine: Implications for the relationship among strain, crystallographic fabric, and seismic anisotropy, *Earth Planet. Sci. Lett.*, *387*, 157–168.

Herring, C. (1950), Diffusional viscosity of a polycrystalline solid, *J. App. Phys.*, *21*(5), 437–445.

Hirth, G., and D. Kohlstedt (1995), Experimental constraints on the dynamics of the partially molten upper mantle 2: Deformation in the dislocation creep regime, *J. Geophys.*

Res., *100*, 15441–15449.

Hirth, G., and D. Kohlstedt (2003), Rheology of the mantle wedge, in *Inside the Subduction Factory*, *Geophys. Monogr. Ser.*, *138*, pp. 83–105.

Jackson, I., U. H. Faul, and R. Skelton (2014), Elastically accommodated grain-boundary sliding: New insights from experiment and modeling, *Phys. Earth and Planet. Inter.*, *228*, 203–210.

Johanesen, K. E., and J. P. Platt (2015), Rheology, microstructure, and fabric in a large scale mantle shear zone, ronda peridotite, southern spain, *J. Struct. Geol.*, *73*, 1–17.

Kaminski, E., and N. Ribe (2001), A kinematic model for recrystallization and texture development in olivine polycrystals, *Earth Planet. Sci. Lett.*, *189*(3-4), 253–267, doi: 10.1016/S0012-821X(01)00356-9.

Keefner, J. W., S. J. Mackwell, D. L. Kohlstedt, and F. Heidelbach (2011), Dependence of dislocation creep of dunite on oxygen fugacity: Implications for viscosity variations in Earth's mantle, *J. Geophys. Res.*.

Langdon, T. (1994), Unified approach to grain boundary sliding in creep and superplasticity, *Acta Metall. Mater.*, *42*, 2437–2443.

Lebensohn, R., and C. Tomé (1993), A self-consistent anisotropic approach for the simulation of plastic deformation and texture development of polycrystals: application to zirconium alloys, *Acta Metallurgica et Materialia*, *41*(9), 2611–2624.

Lee, K.-H., Z. Jiang, and S.-i. Karato (2002), A scanning electron microscope study of the effects of dynamic recrystallization on lattice preferred orientation in olivine, *Tectonophysics*, *351*(4), 331–341.

Mehl, L., and G. Hirth (2008), Plagioclase preferred orientation in layered mylonites: evaluation of flow laws for the lower crust, *J. Geophys. Res.*, *113*(B5), B05202.

Miyazaki, T., K. Sueyoshi, and T. Hiraga (2013), Olivine crystals align during diffusion creep of earth/'s upper mantle, *Nature*, *502*(7471), 321–326.

Nabarro, F. (1948), Deformation of crystals by the motion of single ions, in *Report of a Conference on Strength of Solids*, pp. 75–90.

Platt, J., and W. Behr (2011), Grainsize evolution in ductile shear zones: Implications for strain localization and the strength of the lithosphere, *J. Struct. Geol.*, *33*(4), 537–550.

Poirier, J.-P. (1985), *Creep of crystals: High-temperature deformation processes in metals, ceramics and minerals*, Cambridge University Press, New York.

Précigout, J., and G. Hirth (2014), B-type olivine fabric induced by grain boundary sliding, *Earth Planet. Science Lett.*, *395*, 231–240.

Sachs, G. (1928), Zur ableitung einer fliessbedingung, *Z. Ver. Dtsch. Ing.*, *72*, 734–736.

Schmid, S., J. Boland, and M. Paterson (1977), Superplastic flow in finegrained limestone, *Tectonophysics*, *43*(3-4), 257–291.

Sundberg, M., and R. F. Cooper (2008), Crystallographic preferred orientation produced by diffusional creep of harzburgite: Effects of chemical interactions among phases during plastic flow, *J. Geophys. Res.*, *113*(B12), B12208.

Tommasi, A., D. Mainprice, G. Canova, and Y. Chastel (2000), Viscoplastic self-consistent and equilibrium-based modeling of olivine lattice preferred orientations: Implications for the upper mantle seismic anisotropy, *J. Geophys. Res.*, *105*, 7893–7908.

Toy, V. G., J. Newman, W. Lamb, and B. Tikoff (2010), The role of pyroxenites in formation of shear instabilities in the mantle: Evidence from an ultramafic ultramylonite,

Twin Sisters Massif, Washington, *J. Petrol.*, *51*(1-2), 55.

Underwood, E. (1970), *Quantitative stereology*, Addison-Wesley, Reading, Massachusetts.

Walker, A., E. Rutter, and K. Brodie (1990), Experimental study of grain-size sensitive flow of synthetic, hot-pressed calcite rocks, *Geo. Soc. Lond. Spec. Publ.*, *54*(1), 259.

Wang, Z., Y. Zhao, and D. L. Kohlstedt (2010), Dislocation creep accommodated by grain boundary sliding in dunite, *J. Earth Sci.*, *21*(5), 541–554.

Warren, J. M., and G. Hirth (2006), Grain size sensitive deformation mechanisms in naturally deformed peridotites, *Earth Planet. Sci. Lett.*, *248*(1-2), 438–450.

Wheeler, J. (2009), The preservation of seismic anisotropy in the earth's mantle during diffusion creep, *Geophys. J. Int.*, *178*(3), 1723–1732.

Exp #	σ (MPa)	d (μm)	T (K)	γ	J	$\dot{\varepsilon}_{meas}$ (s^{-1})	$\dot{\varepsilon}_{calc-fabric}$ (s^{-1})	$\dot{\varepsilon}_{calc-uni}$ (s^{-1})	f
PI3-1477$^{\downarrow}$	304	6.3	1473	0.4	1.2	5.60E-05	2.30E-05	2.99E-05	2.4
PI3-1514$^{\downarrow}$	328	20.0	1473	0.1	1.3	1.50E-05	3.10E-05	3.90E-05	0.5
PI3-1519$^{\downarrow}$	290	4.6	1473	0.2	1.3	6.20E-05	2.00E-05	2.54E-05	3.1
PI3-1523$^{\downarrow}$	420	5.4	1473	0.3	1.3	9.80E-05	7.30E-05	9.27E-05	1.3
PI3-1543$^{\downarrow}$	441	16.0	1473	0.4	1.2	7.00E-05	8.60E-05	1.10E-04	0.8
PI3-1166$^{\downarrow}$	240	$\sim$900	1523	0.4	2.7	2.43E-05	3.49E-05	5.01E-05	0.7
PI3-284$^{\rightleftharpoons}$	414	7.0	1473	1.1	1.7	1.70E-04	1.00E-04	5.18E-05	1.7
PI10-941$^{\circlearrowleft}$	227	7.2	1523	1.3	2.4	1.30E-04	2.80E-05	6.32E-06	4.6
PI10-264$^{\circlearrowleft}$	369	3.6	1473	3.5	1.7	1.86E-04	8.50E-05	3.46E-05	2.2
PI10-951$^{\circlearrowleft}$	171	12.1	1523	3.6	5.1	3.60E-05	5.48E-05	2.35E-06	0.7
PI10-951$^{\circlearrowleft}$	177	12.1	1523	4.0	5.2	4.00E-05	5.84E-05	2.65E-06	0.7
PI10-951$^{\circlearrowleft}$	182	11.4	1523	4.3	4.8	4.40E-05	6.32E-05	2.92E-06	0.7
PI10-951$^{\circlearrowleft}$	187	11.5	1523	4.7	5.5	4.70E-05	7.58E-05	3.21E-06	0.6
PI10-951$^{\circlearrowleft}$	191	10.9	1523	5.1	5.3	5.10E-05	7.77E-05	3.45E-06	0.7
PI10-951$^{\circlearrowleft}$	197	11.6	1523	5.5	3.3	5.70E-05	5.86E-05	3.85E-06	1.0
PI10-949$^{\circlearrowleft}$	238	6.8	1523	7.4	2.9	1.90E-04	6.40E-05	7.46E-06	3.0

$^{\downarrow}$triaxial compression $^{\rightleftharpoons}$general shear $^{\circlearrowleft}$torsional shear

Table 1: Table of experimental conditions and results of the micromechanical model. Values of σ and $\dot{\varepsilon}$ are in equivalent terms. Strain in compression experiments was converted to shear strain for comparison. The deformation geometry for each experiment is indicated by the symbols referenced below the table. Data from compression and general shear experiments were previously reported in *Hansen et al.* [2011], *Keefner et al.* [2011], and *Lee et al.* [2002] respectively. All data are from experiments on aggregates of San Carlos olivine, except for PI3-1166, which was from Åheim dunite.

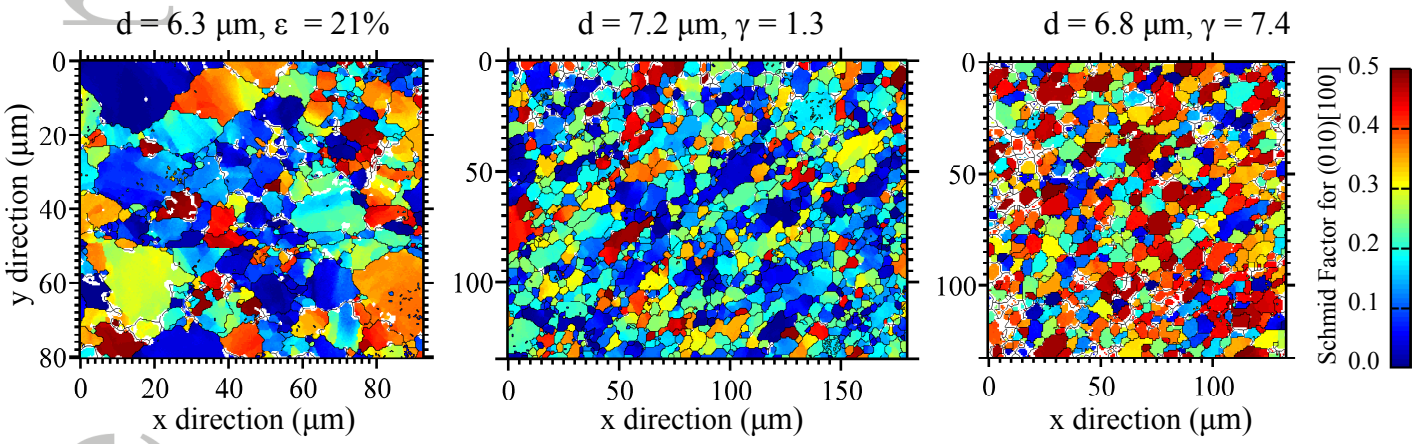

Figure 1: Maps of grains, reconstructed from EBSD data, for samples PI3-1477 (left), PI10-941 (middle), and PI10-949 (right). Colors represent values of Schmid factor calculated for the (010)[100] slip system.

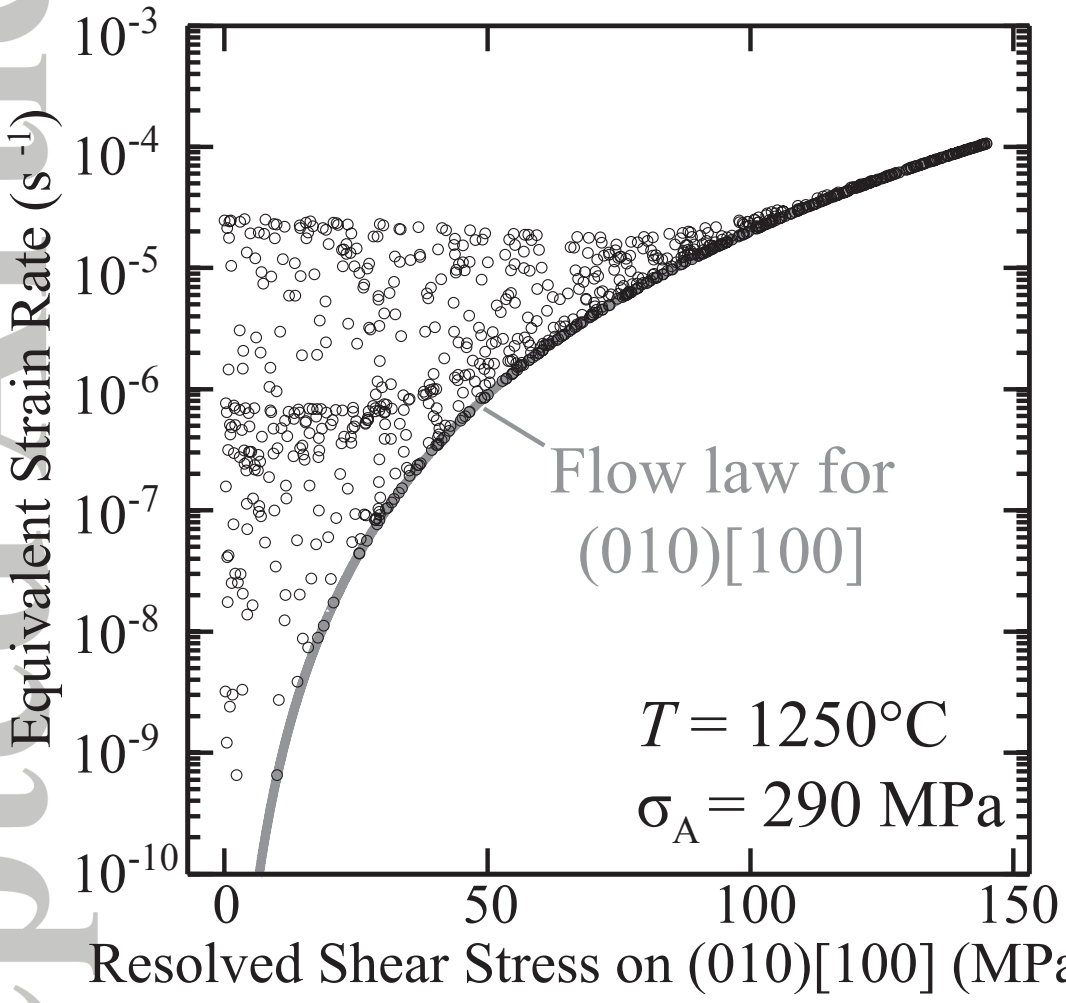

Figure 2: Calculated values of equivalent strain rate for each grain in a compression experiment as a function of resolved shear stress on the (010)[100] slip system.

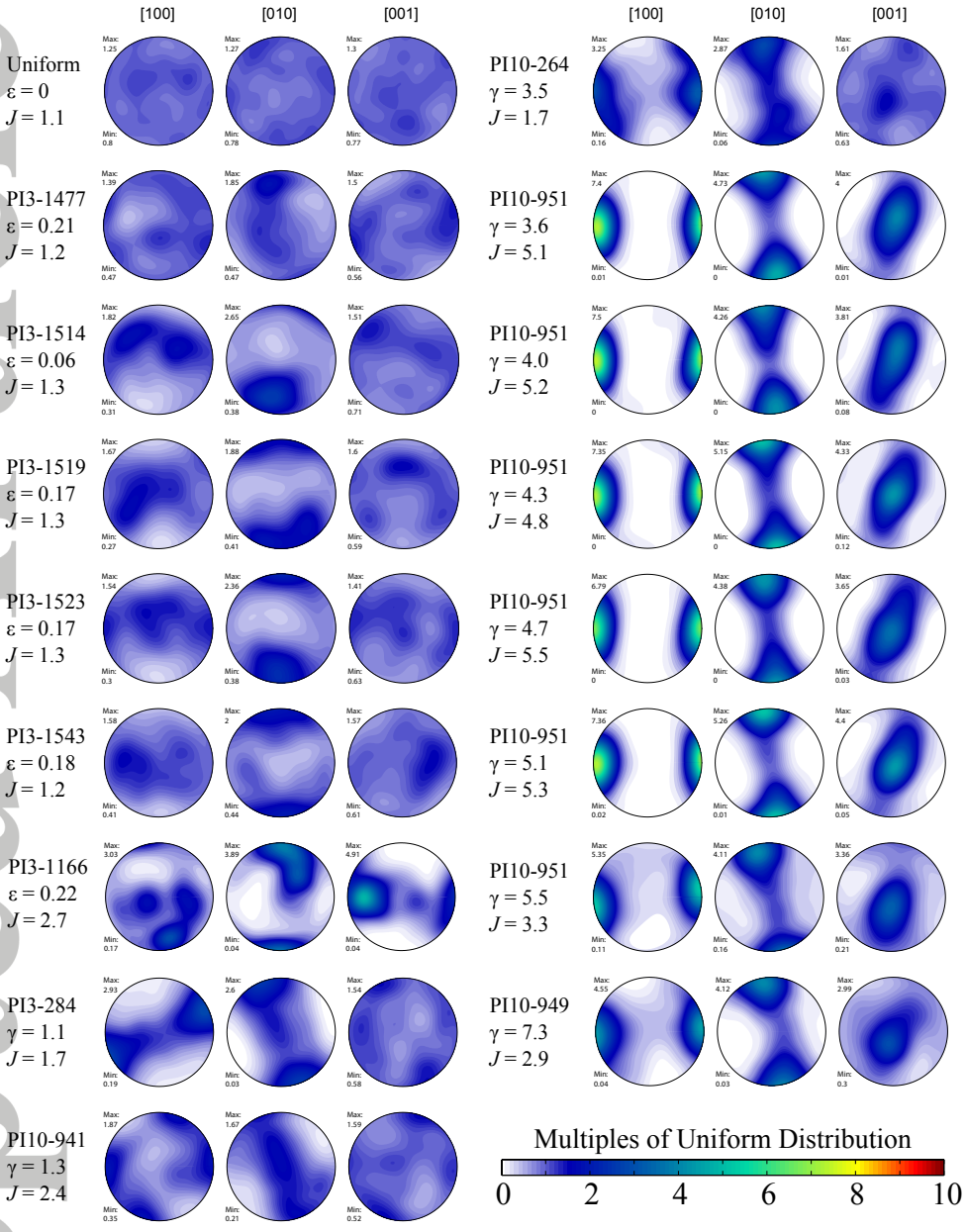

Figure 3: Equal area, lower hemisphere pole figures generated from EBSD measurements for each data set used in the micromechanical models. Values of multiples of uniform distribution are represented by the color scale. All of the experiments labeled with a PI3 prefix were carried out in triaxial compression, with the exception of PI3-284, which was carried out in general shear. The experiments preformed using PI10 were carried out in torsional shear. The orientation of maximum compression is to the north for pole figures from compression experiments and the direction of shear is top to the right for pole figures from shear experiments.

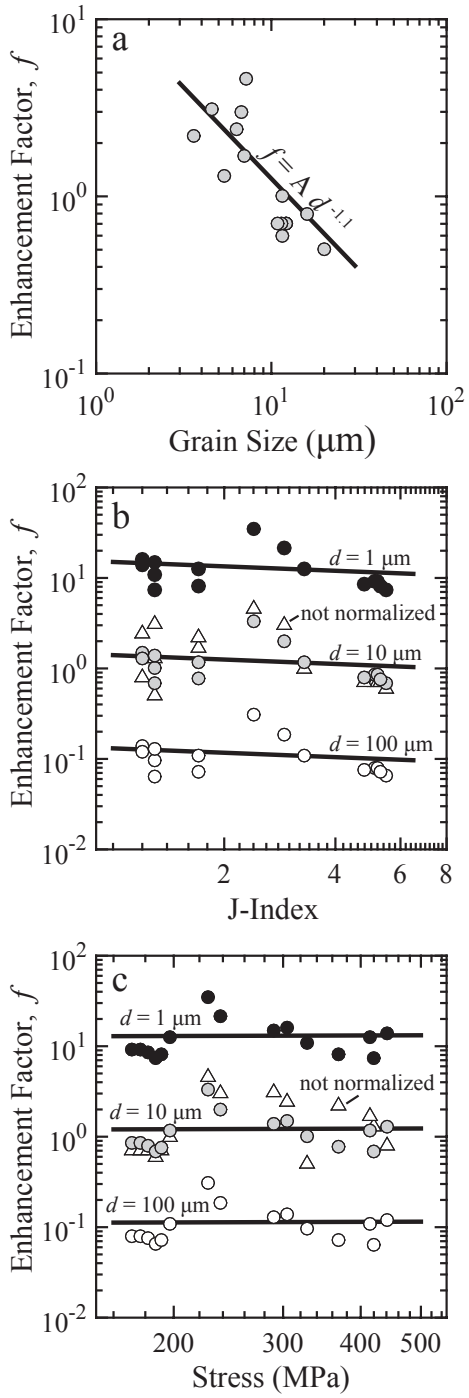

Figure 4: (a) Strain rate enhancement factor (f) as a function of grain size of olivine aggregates. The line is a least squares fit of the data represented by Equation 16. (b) f as a function of J index. (c) f as a function of equivalent stress. The values of f in plots (b) and (c) were normalized to grain sizes of 1 (black circles), 10 (grey circles), and 100 μm (white circles) using Equation 16 and the triangles represent non-normalized values. The lines in (b) and (c) are least square fits of grain-size normalized values of f as function of J-index or stress. The results indicate that, at constant grain size, f is independent of J-index and stress with $f \propto J^{-0.2\pm0.5}$ and $f \propto \sigma^{0.0\pm1.0}$.

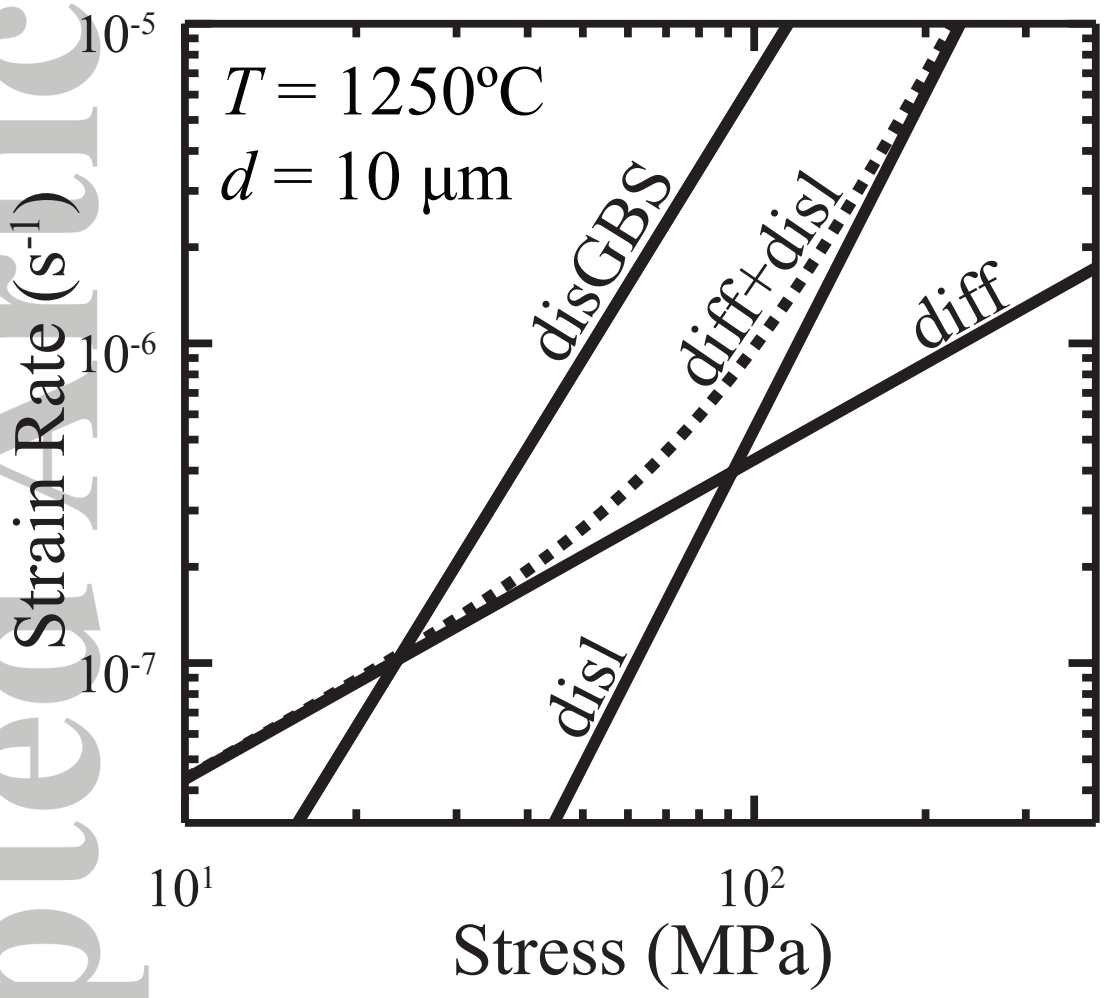

Figure 5: Strain rate as a function of stress with flow laws for diffusion creep (diff) and dislocation creep (disl) from *Hirth and Kohlstedt* [2003] and dislocation-accommodated grain boundary sliding (disGBS) from *Hansen et al.* [2011] at conditions typical of laboratory experiments. The dashed line is a sum of the strain rates from the diffusion and dislocation creep flow laws.

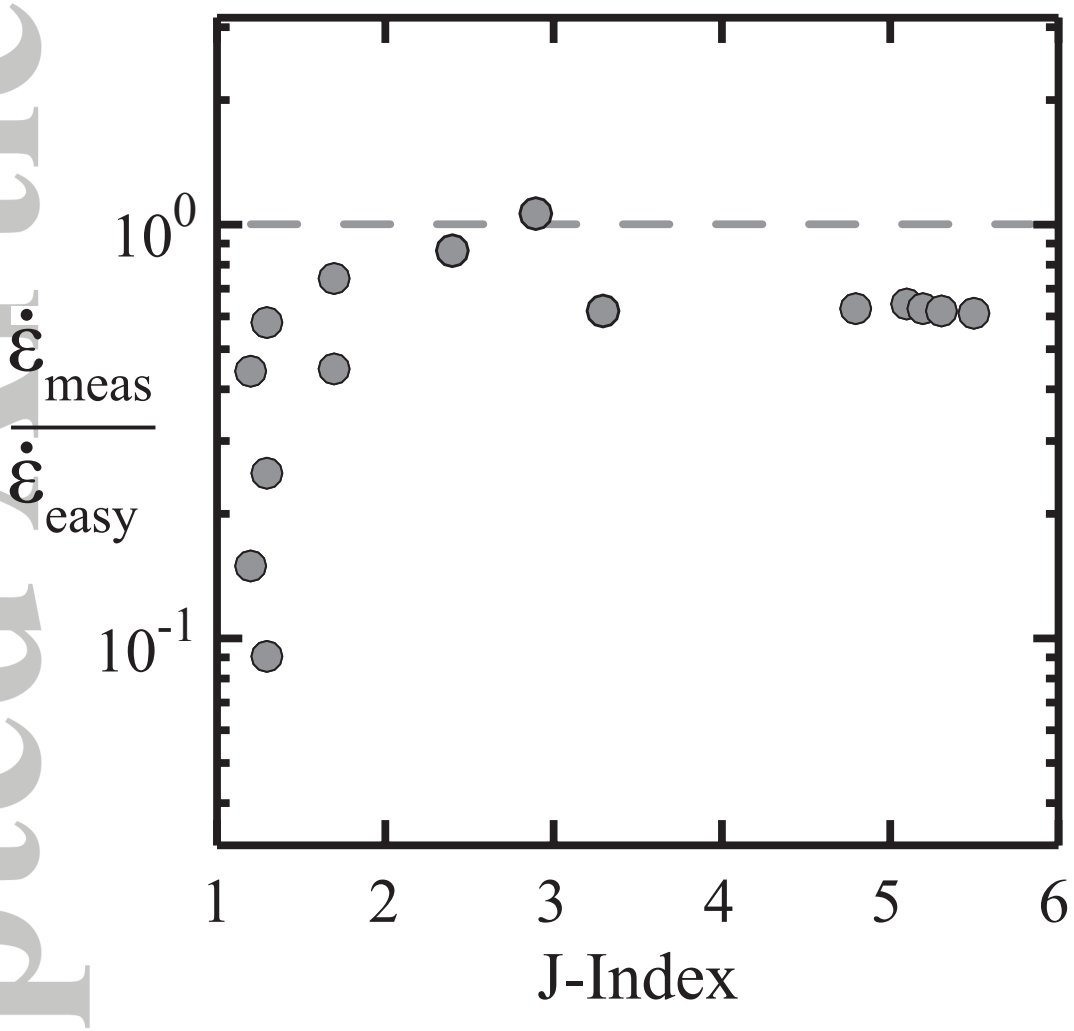

Figure 6: Ratio of measured strain rate of olivine aggregates to the strain rate for the flow law for single crystals in the $[110]_c$ orientation from *Bai et al.* [1991] as a function of J-index. Conditions at which the measured strain rate is equal to the flow law for the easy slip system are indicated by the horizontal dashed line.